Inverse design of constituent materials of 3D hybrid woven composites for tailored effective properties using reduced order model and genetic algorithm

Shilian Sun[a], Weijie Zhang[a], Ying Yan[a], Xi Zou[b], Shibo Yan[a,1]

[a]*School of Aeronautic Science and Engineering, Beihang University, Beijing, 100191, China*
[b]*Department of Aerospace Engineering, Swansea University, Swansea, SA1 8EN, United Kingdom*

Abstract

3D woven hybrid composites can exhibit superior mechanical performance compared to non-hybrid counterparts, due to synergistic effects arising from the combination of fibres with different properties. However, the design space of such materials expands exponentially with the number of yarns and candidate fibre types, rendering trial-and-error approaches impractical for identifying a global optimum within this vast parameter space. In this work, we propose an efficient inverse design framework for tailoring the effective properties of 3D woven hybrid composites through the selection of constituent materials. The framework integrates a genetic algorithm as an optimiser to automatically search for optimal constituent material combinations, while employing a reduced order model generated by the proper generalised decomposition method as a rapid forward predictor of effective properties during iterations. The proposed inverse design framework was verified through a case study on 3D hybrid orthogonal woven composites, involving a design space of one million potential combinations of constituent materials. The computational time of material characterisation in the inverse design framework results in an acceleration of approximately 122 times compared to the conventional numerical homogenisation in the case study. The results confirm the framework's ability to efficiently navigate vast design spaces to identify optimal solutions with high computational performance. *Keywords:* Inverse design, effective properties, 3D hybrid woven composites, reduced order model, genetic algorithm

1. Introduction

3D woven composites have garnered increasing interest in the aerospace sector due to their exceptional out-of-plane mechanical properties and remarkable near-net-shape capability compared to conventional laminates [1, 2]. The most notable applications of 3D woven composites include the fan blades and the fan case

[1] Corresponding author
Email address: shiboyan@buaa.edu.cn (Shibo Yan)

of LEAP engine [3]. To further enhance their advantages, by using two or more types of fibre in the weaving process, 3D hybrid woven composites offer significantly more design space than non-hybrid ones [4]. By leveraging the synergetic effects of the mechanical properties of different fibres, such as high-strength carbon fibre and high-toughness aramid fibre, the mechanical performance of 3D hybrid woven composites can be tailored by intelligent combinations of different fibres within the preforms with respect to specific load conditions of the composites [5], e.g. increased fracture strain [6], enhanced bending strength [7] and higher damage tolerance [8]. In addition, the fan blades of GE9X were reported to integrate 5-10% glass fibres, aiming to improve their resistance to bird strikes [9].

Compared to their non-hybrid counterparts, the design space of 3D hybrid woven composites expands exponentially with the number of yarns in the material and the candidate fibres (such as carbon, aramid and glass fibres of different modulus, strength, toughness, and even cost). For example, for a hybrid composite with 12 yarns in its unit cell, there will potentially be 1.0×10^{12} constituent material combinations, (called *hybridisations*) if 10 different fibres are considered. The trial-and-error approach is impractical for identifying a global optimum within such a vast design space, regardless of whether it employs experimental studies [7, 10, 11] or advanced numerical simulations [12, 13] for material characterisation. Recently, some promising design strategies for 3D woven composites have been presented for bending stiffness [14] and effective properties [15]. Despite Sitnikova et al. [15] have proposed a design strategy for effective properties to replace the trial-and-error method, employing three key properties of the weave as design parameters, the computational process would encounter challenges due to the reliance on conventional multiscale simulations for forward prediction (material characterisation). Therefore, for the design of 3D hybrid woven composites to be possible, an inverse design framework [16, 17], which starts with the desired mechanical performance and works backward to identify the optimal hybridisations, relying simultaneously on optimisation algorithms and efficient tools for forward prediction, is one of the potential solutions.

Recently, several optimisation algorithms have been successfully used to address optimisation problems in 3D woven composites, including the particle swarm algorithm [18] for weight reduction, the artificial bee colony algorithm [19] for maximising elastic properties, and the genetic algorithm [20] for minimising residual stress and process time. Particle swarm algorithm is particularly effective in solving continuous optimisation problems due to its ability to achieve rapid convergence and adaptability to various problem landscapes, and the artificial bee colony algorithm demonstrates superior performance in handling complex, nonlinear, and multimodal optimisation problems. A genetic algorithm is particularly well suited for application in an inverse design framework for woven composites, since the discrete combination of constituent materials inherently aligns with the unique strengths of the genetic algorithm [21] (optimising the discrete combination problems).

To improve design efficiency, machine learning [22, 23] has been effectively employed to develop surrogate models to replace the conventional multiscale method in forward prediction. However, the performance of machine learning may depend heavily on the quality and variability of the training data. In contrast, model order reduction techniques are built on the foundation of numerical models and strict mathematical principles, avoiding the dependency of training data. In the context of model order reduction, the evaluation of *a posteriori* methods such as reduced basis (RB) [24, 25] and proper orthogonal decomposition (POD) [26] hinges on the establishment of reduced bases (a.k.a. modes). Unlike those aforementioned methods, proper generalised decomposition (PGD) [27, 28, 29] is an *a priori* method that approximates a multi-parameter state solution as a sum of products of lower-parameter modes, making it particularly effective in addressing the curse of dimensionality. A PGD-based reduced order model incorporates *a priori* information about those design parameters (fibre properties), enabling fast forward prediction of different hybridisations in an online phase. Thus, it is particularly well suited for engineering design applications that require extensive repetitive simulations and optimisations, such as real-time prediction of the stiffness of 2D woven composites [30] and optimisation of fibre orientations in laminated composites [31].

As 3D hybrid woven composites are used mainly as thin-walled structures in the aerospace sector, their in-plane effective properties must be addressed before designing the out-of-plane mechanical properties. This is because the optimised stiffness is critical not only for load transfer and deformation control but also for preventing stability-driven failures like buckling. Although previous studies [15] have attempted on the stiffness design of woven composites, computational efficiency remains a significant challenge, particularly for those 3D hybrid woven composites with enormous hybridisations. A rapid methodology to tailor the stiffness properties of 3D woven composites within a vast design space would shorten the design cycle and promote the engineering application of these composites. Furthermore, the synergistic effects of mechanical properties from different fibre types have not been sufficiently considered in the existing literature. To enhance computational efficiency and capitalise on the synergistic effects of diverse fibre types, we propose an efficient inverse design framework to tailor the effective properties of 3D hybrid woven composites through the selection of constituent materials. Within this framework, we employ a genetic algorithm as an optimiser to automatically search for optimal hybridisations and utilise a PGD-based reduced order model as a rapid predictor for effective properties.

The article is structured as follows. Section 2 introduces the conventional multiscale method commonly employed to simulate the effective properties of various hybridisations. In Section 3, the process of generating a reduced order model through the PGD method based on conventional multiscale characterisation is detailed, along with the description of a genetic algorithm used as an optimiser within the inverse design framework. To demonstrate the validity of the proposed inverse design framework, Section 4 presents a case study on 3D hybrid orthogonal woven composites.

2. Conventional multiscale method for forward prediction of effective properties

In this section, we present a conventional multiscale computational framework for forward prediction of effective properties of 3D hybrid woven composites, from which a PGD-based reduced order model will be developed. At the microscale, a homogenisation analysis is performed to characterise the material properties of each yarn. Based on this, a unit cell is used at the mesoscale to determine the effective properties of 3D hybrid woven composites. Specifically, the relative displacement (a.k.a. periodic) boundary conditions are applied to the unit cell [32], and the corresponding results are obtained through the standard computational homogenisation procedure [33] based on the finite element method (FEM).

2.1. Analytical homogenisation at microscale

At the microscale, the effective properties of the yarn are generally considered as a homogenised unidirectional composite with transverse isotropy, and its stiffness properties can be calculated using either micromechanical analytical solutions or a unit cell model. Among the analytical ones, the Chamis [34] model is widely employed to calculate the stiffness properties of a homogenised yarn, with the corresponding equations provided in Eq.(1).

$$\hat{E}_1 = V^{\mathrm{f}} E_1^{\mathrm{f}} + (1 - V^{\mathrm{f}}) E^{\mathrm{m}}, \qquad \hat{E}_2 = \hat{E}_3 = \frac{E^{\mathrm{m}}}{1 - \sqrt{V^{\mathrm{f}}}\left(1 - \frac{E^{\mathrm{m}}}{E_2^{\mathrm{f}}}\right)},$$

$$\hat{G}_{12} = \hat{G}_{13} = \frac{G^{\mathrm{m}}}{1 - \sqrt{V^{\mathrm{f}}}\left(1 - \frac{G^{\mathrm{m}}}{G_{12}^{\mathrm{f}}}\right)}, \qquad \hat{G}_{23} = \frac{G^{\mathrm{m}}}{1 - \sqrt{V^{\mathrm{f}}}\left(1 - \frac{G^{\mathrm{m}}}{G_{23}^{\mathrm{f}}}\right)}$$

$$\hat{\nu}_{23} = \frac{\hat{E}_2}{2\hat{G}_{23}} - 1, \tag{1}$$

$$\hat{\nu}_{12} = \hat{\nu}_{13} = V^{\mathrm{f}} \nu_{12}^{\mathrm{f}} + (1 - V^{\mathrm{f}}) \nu^{\mathrm{m}},$$

where $E_1^{\mathrm{f}}, E_2^{\mathrm{f}}, \nu_{12}^{\mathrm{f}}, G_{12}^{\mathrm{f}}$ and G_{23}^{f} represent the elastic properties of the fibre; E^{m} and ν^{m} denote the elastic properties of the matrix; $\hat{E}_1, \hat{E}_2, \hat{E}_3, \hat{\nu}_{12}, \hat{\nu}_{13}, \hat{\nu}_{23}, \hat{G}_{12}, \hat{G}_{13}$ and $\hat{G}_{23}$ are the elastic properties of a yarn; and V^{f} is the intra-yarn fibre volume fraction. The elastic properties of some typical fibres used for aerostructures are summarised in Table 1 and will be considered as potential options for 3D hybrid woven composites in this paper. If certain elastic properties are not available, "educated guess" [35] is utilised to estimate these properties in the present stage. Based on trends observed in fibres with complete datasets (e.g., T300 and T800), the ratios $E_2/E_1 = 0.04 \sim 0.06$ and $G_{12}/E_2 = 0.65 \sim 1.08$. For T1100 and M40JB, we assumed that $E_2 = 0.059E_1$ and $G_{12} = 0.86E_2$, respectively. For M46JB, M50JB, and M55JB, the transverse modulus and in-plane shear modulus were chosen as $E_2 = 0.046E_1$ and $G_{12} = 20.0$ GPa, respectively, to prevent the

shear stiffness G_{12} from being unrealistically high [36]. Furthermore, for all the aforementioned material types, the in-plane Poisson's ratios ν_{12} and ν_{23} were assumed to be identical to those of T800 and T300, with $G_{23} = 0.4E_2$. It should be noted that these data based on the "educated guess" are intended only as representative examples; the methodology itself is independent of these values, and users may employ more realistic data as needed. As reported in [37, 38, 39], conventional epoxy resin systems for aerospace applications exhibit stiffness values ranging from 3.2 to 4.0 GPa, which are substantially lower than the stiffness values of most fibres listed in Table 1. The shear modulus of a yarn, when calculated using Eq.(1), demonstrates relatively minor variations across different epoxy resin systems. Given that these variations are minimal, only one type of epoxy resin is selected for this investigation for simplification as given in Table 1.

Table 1: Elastic properties of candidate constituent materials (Unit for moduli: GPa).

Material		E_1	E_2	ν_{12}	ν_{23}	G_{12}	G_{23}	Filament diameter (mm)
Standard modulus fibre	T300 [46, 47]	230	13.8	0.2	0.25	9.0	5.5	0.007[47]
High strength fibre	T800 [10, 47]	294	17.2	0.2	0.25	18.6	6.9	0.005[47]
	T1100 [47]	324	19.4*	0.2*	0.25*	16.2*	7.8*	0.005[47]
High modulus fibre	M40JB [47]	377	22.6*	0.2*	0.25*	18.9*	9.0*	0.005[47]
	M46JB [47]	436	20.0*	0.2*	0.25*	20.0*	8.0*	0.005[47]
	M50JB [47]	475	22.0*	0.2*	0.25*	20.0*	8.8*	0.005[47]
	M55JB [47]	540	25.0*	0.2*	0.25*	20.0*	10.0*	0.005[47]
High toughness fibre	E-glass [40]	70	70	0.2	0.2	29.2	29.2	0.007[41, 42]
	S-glass [43, 44]	87	87	0.23	0.23	35.4	35.4	0.007[42, 43]
	Kevlar49 [10]	112	112	0.36	0.36	41.2	41.2	0.012[45]

Matrix	Prime 20LV [39]	3.5	0.35	-	-

∗ Assumed value

2.2. Computational homogenisation at mesoscale

At the mesoscale, due to the complexity of the geometric configurations, the effective properties of 3D hybrid woven composites are typically derived from a computational homogenisation approach. For a cuboid unit cell, to characterise translational symmetry or periodicity, the Dirichlet boundary conditions are applied in a convenient Cartesian coordinates as follows [32]:

$$\begin{bmatrix} u' \\ v' \\ w' \end{bmatrix} - \begin{bmatrix} u \\ v \\ w \end{bmatrix} = \begin{bmatrix} \varepsilon_{0x} & \gamma_{xy0} & \gamma_{xz0} \\ 0 & \varepsilon_{0y} & \gamma_{yz0} \\ 0 & 0 & \varepsilon_{0z} \end{bmatrix} \begin{bmatrix} \Delta x \\ \Delta y \\ \Delta z \end{bmatrix}, \tag{2}$$

where u,v,w and u',v',w' are the mesoscale displacement components at corresponding points on the symmetry faces of the unit cell; $\{\varepsilon_x^0, \varepsilon_y^0, \varepsilon_z^0, \gamma_{xy}^0, \gamma_{yz}^0, \gamma_{xz}^0\}$ are macroscopic engineering strains of the unit cell; $[\Delta x,\Delta y,\Delta z]^T$ is the translation vector associated with the translational symmetry.

In terms of finite element implementation of the boundary conditions, the six macroscopic engineering strains are introduced as independent key degrees of freedom through six corresponding dummy nodes that are not part of the physical mesh, with the macroscopic strains imposed as prescribed "displacements" of these nodes. The reaction quantities associated with these dummy nodes are not physical nodal forces but generalized forces that are energetically conjugate to the imposed macroscopic strain components. These quantities correspond to the volume integral of the microscopic stress field, i.e. $\int_\Omega \sigma_{ij}\, d\Omega$, and therefore have the physical dimension of force×length, more details about this implementation technique are given in [32].

The linear algebraic form of the finite element model reads

$$\begin{aligned} \mathbf{Ku} &= \mathbf{f} + \mathbf{r}, \\ \mathbf{Cu} &= \mathbf{0}, \end{aligned} \tag{3}$$

where **K** is the stiffness matrix relating the unit cell dimensions, mesh element type and element count, **C** is the linear constraint matrix that enforces the boundary conditions, and **u**, **f** and **r** are vectors denoting the nodal displacement, external force, and reaction force, respectively. It should be noted that the solution vector **u** denotes an augmented vector, which consists of both physical nodal displacements and additional "displacements" associated with dummy nodes.

Remark 1. Due to their geometric configurations, 3D hybrid woven composites lack translational symmetry in *z*-direction [48]. Consequently, the relative displacement boundary conditions for the unit cell are only enforced in the *x*-*y* plane. Thus, only three key degrees of freedom that represent the macroscopic engineering strains ε_x^0, ε_y^0 and γ_{xy}^0 are required to be appended to the mesoscale displacement vector **u**.

Remark 2. Several approaches, including the transformation method [49], penalty method [50], and Lagrange multiplier-based method [51], can be adopted to solve the problem described in Eq.(3).

The global system of equations can be solved with standard static condensation, which partitions the system according to the boundary conditions.

$$\begin{bmatrix} \mathbf{K}_{\mathrm{E}} & \mathbf{K}_{\mathrm{EF}} \\ \mathbf{K}_{\mathrm{TEF}} & \mathbf{K}_{\mathrm{F}} \end{bmatrix} \begin{bmatrix} \bar{\mathbf{u}}_{\mathrm{E}} \\ \mathbf{u}_{\mathrm{F}} \end{bmatrix} = \begin{bmatrix} \mathbf{r}_{\mathrm{E}} \\ \mathbf{0} \end{bmatrix}. \tag{4}$$

In particular, as shown in Eq.(4), the subscript E is associated with nodes where displacements are known (E stands for *essential*), whereas subscript F denotes the free nodes. In this work, no external forces are applied, thus **f** = 0. Here $\bar{\mathbf{u}}_{\mathrm{E}}$ represents the known displacement, and $\mathbf{u}_{\mathrm{F}}$ denotes the unknown nodal displacement; $\mathbf{r}_{\mathrm{E}}$ represents the reaction force; and the stiffness matrix is subdivided into submatrices $\mathbf{K}_{\mathrm{E}}$,$\mathbf{K}_{\mathrm{EF}}$ and $\mathbf{K}_{\mathrm{F}}$ that correspond to this partition.

By solving Eq.(4), the unknown nodal displacement and reaction force can be obtained as $\mathbf{K}_{\mathrm{T}}\bar{\mathbf{u}}$

$$\begin{cases} \mathbf{u}_{\mathrm{F}} = -\mathbf{K}_{\mathrm{F}}^{-1} \mathbf{K}_{\mathrm{EF}} \mathbf{u}_{\mathrm{E}} \\ \mathbf{r}_{\mathrm{E}} = \mathbf{K}_{\mathrm{E}}\bar{\mathbf{u}}_{\mathrm{E}} + \mathbf{K}_{\mathrm{EF}}\mathbf{u}_{\mathrm{F}} \end{cases} \tag{5}$$

To obtain the four independent effective properties E_x^{eff},ν_{xy}^{eff},E_y^{eff}, and G_{xy}^{eff} that are involved in the unit cell, three uniaxial stress load cases are required, which are prescribed through the corresponding macroscale strain associated with a key degree of freedom, and strains in other directions are left free from constraints to ensure a uniaxial tension or pure shear stress state:

1. Load case I: applying uniaxial tension in *x*-direction, $\varepsilon_{x,\mathrm{I}}^0 = 0.01$. This will obtain E_x^{eff} and ν_{xy}^{eff}.
2. Load case II: applying uniaxial tension in *y*-direction, $\varepsilon_{y,\mathrm{II}}^0 = 0.01$. This will obtain E_y^{eff}.
3. Load case III: applying pure shear in *xy* plane, $\gamma_{xy,\mathrm{III}}^0 = 0.01$. This will obtain G_{xy}^{eff}.

For each load case, the partition of the global system of equations in Eq.(4) is distinct. The strains are applied in the form of displacements at the key degrees of freedom and are incorporated into the known nodal displacement vectors $\bar{\mathbf{u}}_{\mathrm{E,I}}$,$\bar{\mathbf{u}}_{\mathrm{E,II}}$ and $\bar{\mathbf{u}}_{\mathrm{E,III}}$, respectively. Subsequently, the reaction force vectors for the three load cases $\mathbf{r}_{\mathrm{E,I}}$,$\mathbf{r}_{\mathrm{E,II}}$ and $\mathbf{r}_{\mathrm{E,III}}$ can be calculated using Eq.(5). From these reaction force vectors, we can extract the nodal reaction force $R_{x,\mathrm{I}}$,$R_{y,\mathrm{II}}$ and $R_{xy,\mathrm{III}}$, corresponding to each load case. Here, $R_{x,\mathrm{I}}$, $R_{y,\mathrm{II}}$ and $R_{xy,\mathrm{III}}$ denote generalised reaction quantities

associated with the imposed macroscopic strain parameters, rather than conventional nodal reaction forces. In particular, the extraction can be expressed as

$$\begin{aligned} R_{x,\mathrm{I}} &\in \mathbf{r}_{\mathrm{E,I}}; & \mathbf{r}_{\mathrm{E,I}} &= \mathbf{K}_{\mathrm{E,I}}\bar{\mathbf{u}}_{\mathrm{E,I}} + \mathbf{K}_{\mathrm{EF,I}}\mathbf{u}_{\mathrm{F,I}}; \\ R_{y,\mathrm{II}} &\in \mathbf{r}_{\mathrm{E,II}}; & \mathbf{r}_{\mathrm{E,II}} &= \mathbf{K}_{\mathrm{E,II}}\bar{\mathbf{u}}_{\mathrm{E,II}} + \mathbf{K}_{\mathrm{EF,II}}\mathbf{u}_{\mathrm{F,II}}; \\ R_{xy,\mathrm{III}} &\in \mathbf{r}_{\mathrm{E,III}}; & \mathbf{r}_{\mathrm{E,III}} &= \mathbf{K}_{\mathrm{E,III}}\bar{\mathbf{u}}_{\mathrm{E,III}} + \mathbf{K}_{\mathrm{EF,III}}\mathbf{u}_{\mathrm{F,III}}. \end{aligned} \tag{6}$$

To characterise the homogenised effective macroscopic response, the classic Hill-Mandel theory [52] is adopted. It should be noted that the unit cell model is assumed to have perfect fibre-matrix interfaces in this study. The macroscopic stress tensor σ^0 is obtained as a volume average of its mesoscopic counterpart σ by

$$\boldsymbol{\sigma}^0 := \langle \boldsymbol{\sigma} \rangle_\Omega = \frac{1}{V}\int_\Omega \boldsymbol{\sigma}\, \mathrm{d}\Omega = \frac{1}{V}\int_\Omega \boldsymbol{\nabla}\cdot(\boldsymbol{\sigma}\otimes \boldsymbol{x})\mathrm{d}\Omega = \frac{1}{V}\int_{\partial\Omega} \boldsymbol{t}\otimes \boldsymbol{x}\mathrm{d}\Gamma, \tag{7}$$

where Ω denotes the domain of the unit cell, $t = \sigma n$ is the surface traction on the boundary faces of the unit cell $\Gamma = \partial\Omega$, and n is the unit normal. $V = \int_\Omega \mathrm{d}\Omega$ represents the volume of the unit cell. Particularly, in the three load cases, the integral of surface tractions is the reaction force at the corresponding key degrees of freedom. Thus we have

$$\begin{aligned} \sigma^0_{x,\mathrm{I}} &= \frac{R_{x,\mathrm{I}}}{V}; \\ \sigma^0_{y,\mathrm{II}} &= \frac{R_{y,\mathrm{II}}}{V}; \\ \tau^0_{xy,\mathrm{III}} &= \frac{R_{xy,\mathrm{III}}}{V}. \end{aligned} \tag{8}$$

Then, the four independent effective properties of the unit cell can be determined through

$$\begin{aligned} E^{\mathrm{eff}}_x &= \frac{\sigma^0_{x,\mathrm{I}}}{\varepsilon^0_{x,\mathrm{I}}}, & \varepsilon^0_{y,\mathrm{I}} &\in \mathbf{u}_{\mathrm{F}} \\ \nu^{\mathrm{eff}}_{xy} &= -\frac{\varepsilon^0_{y,\mathrm{I}}}{\varepsilon^0_{x,\mathrm{I}}}, & \text{where,I;}^{\mathrm{II}} & \\ E^{\mathrm{eff}}_y &= \frac{\sigma^0_{y,\mathrm{II}}}{\varepsilon^0_{y,\mathrm{II}}}; \\ G^{\mathrm{eff}}_{xy} &= \frac{\tau^0_{xy,\mathrm{III}}}{\gamma^0_{xy,\mathrm{III}}} \end{aligned} \tag{9}$$

In addition, the effective Poisson's ratio ν^{eff}_{yx} can be calculated as

$$\nu^{\mathrm{eff}}_{yx} = \frac{E^{\mathrm{eff}}_y}{E^{\mathrm{eff}}_x}\nu^{\mathrm{eff}}_{xy}. \tag{10}$$

From Eq.(9), it is demonstrated that the macroscopic effective properties can be calculated from the mesoscopic responses on the key degrees of freedom under these load cases. For more detailed discussions, the readers are kindly referred to the literature such as [32].

3. Inverse design framework for constituent materials of 3D hybrid woven composites

In this section, the novel inverse design framework for constituent materials of 3D hybrid woven composites with tailored effective properties is described in detail.

In a conventional design optimisation that involves multiscale homogenisation computation, the calculation of the macroscopic effective properties of a material is expensive as it requires repeatedly solving the implicit problem described in Eq.(3). This trial-and-error approach will become prohibitively unaffordable when the dimension of design space becomes large, causing the so-called "curse of dimensionality".

To address this problem and enhance the computational efficiency, in this paper, a reduced order model is generated by the PGD method based on the mesoscale finite element model in an offline phase. Then the reduced order model serves as a rapid online generator of effective properties for various hybridisations of the composites with a multidimensional parameter space. Afterwards, the online reduced order model is integrated into a genetic algorithm, which functions as an optimiser to identify the hybridisations of 3D woven composites whose effective properties satisfy the user tailored inputs. An overview of the inverse design framework is illustrated in Figure 1. In this flowchart, the development of the reduced order model in the offline phase is detailed in Subsection 3.1.2; the encapsulated procedure of the reduced order model for online phase is described in Subsection 3.1.3, and the workflow of the application of the online phase in the genetic algorithm is presented in Subsection 3.2.

3.1. Reduced order model generated by the proper generalised decomposition method

In order to analyse the multidimensional design space, we attempt to separate the material properties of each yarn from the global stiffness matrix. With these material properties serving as parametric variables, a

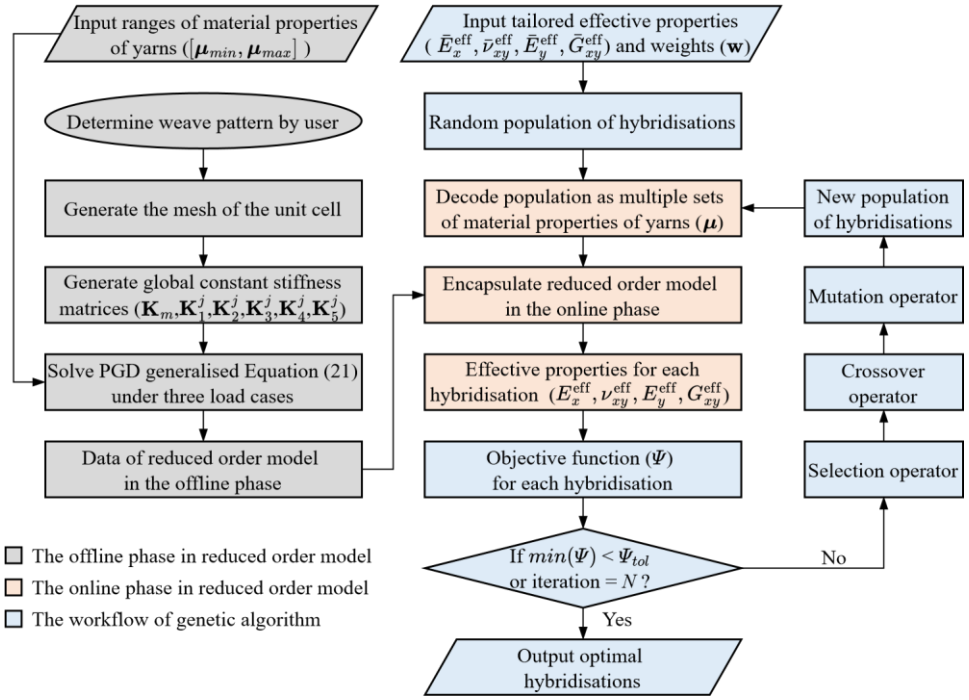

Figure 1: The workflow of the proposed inverse design framework for a given weave pattern.

reduced order model is obtained by the PGD method to enhance the computational efficiency of obtaining the homogenised effective properties. A typical reduced order modelling process can be divided into an offline and an online phase. During the offline phase, the PGD method exploits the parameter space to establish a reduced basis or *modes*, which contains the essential information of all the possible material selections for each yarn in the 3D hybrid woven composites. In the online phase, these modes are encapsulated as a rapid generator to obtain the effective properties with arbitrary combinations of material properties for each yarn as the input.

3.1.1. Separation of material properties in global stiffness matrix

At the mesoscale, the yarns of a 3D hybrid woven composite, whose material properties calculated from Eq.(1), are all homogenised as transversely isotropic materials, while the resin is typically considered as an isotropic material. For a transversely isotropic material, its elastic matrix **D** is typically represented by a 6 × 6 symmetric matrix

$$\mathbf{D} = \begin{bmatrix} E_1 + 4\kappa_{23}\nu_{12}^2 & 2\kappa_{23}\nu_{12} & 2\kappa_{23}\nu_{12} & 0 & 0 & 0 \\ 2\kappa_{23}\nu_{12} & \kappa_{23} + G_{23} & \kappa_{23} - G_{23} & 0 & 0 & 0 \\ 2\kappa_{23}\nu_{12} & \kappa_{23} - G_{23} & \kappa_{23} + G_{23} & 0 & 0 & 0 \\ 0 & 0 & 0 & G_{12} & 0 & 0 \\ 0 & 0 & 0 & 0 & G_{12} & 0 \\ 0 & 0 & 0 & 0 & 0 & G_{23} \end{bmatrix}, \tag{11}$$

where κ_{23} is the in-plane bulk modulus calculated by

$$\frac{1}{\kappa_{23}} = \frac{2(1-\nu_{23})}{E_2} - \frac{4\nu_{12}^2}{E_1}; \tag{12}$$

E_1,E_2,ν_{12},ν_{23},G_{12} and G_{23} are the engineering elastic properties of the material. Note that the material elastic matrix $\mathbf{D}$ can be decomposed into

$$\mathbf{D} = 2\kappa_{23}\nu_{12}\mathbf{D}_1 + (E_1 + 4\kappa_{23}\nu_{12}^2)\mathbf{D}_2 + \kappa_{23}\mathbf{D}_3 + G_{12}\mathbf{D}_4 + G_{23}\mathbf{D}_5, \tag{13}$$

where $\mathbf{D}_1$,$\mathbf{D}_2$,$\mathbf{D}_3$,$\mathbf{D}_4$ and $\mathbf{D}_5$ are constant matrices. Note that Eq.(13) is applicable to all yarns.

In this paper, for simplicity, the resin matrix is considered a fixed type of isotropic material. This implies a constant contribution from the resin to the overall stiffness of the unit cell.

When the weave pattern of a unit cell is determined, a finite element model of the unit cell is established with a convergent mesh size. After the discretisation, the local stiffness matrix of an element $\mathbf{K}^e$ is calculated by

$$\mathbf{K}^e = \int_{\Omega_e} \mathbf{B}^{e\mathrm{T}}\mathbf{D}\mathbf{B}^e \,\mathrm{d}\Omega = 2\kappa_{23}^e\nu_{12}^e\mathbf{K}_1^e + [E_1^e + 4\kappa_{23}^e(\nu_{12}^e)^2]\mathbf{K}_2^e + \kappa_{23}^e\mathbf{K}_3^e + G_{12}^e\mathbf{K}_4^e + G_{23}^e\mathbf{K}_5^e, \tag{14}$$

where $\mathbf{B}^e$ denotes the strain-displacement matrix of an element e with its domain Ω^e; $\nu_{12}^e, E_1^e, \kappa_{23}^e, G_{12}^e$ and G_{23}^e are material properties of the element, and $\mathbf{K}_1^e, \mathbf{K}_2^e, \mathbf{K}_3^e, \mathbf{K}_4^e$ and $\mathbf{K}^e{}_5$ are constant stiffness-like matrices of the element, which are integrated by

$$\mathbf{K}_a^e = \int_{\Omega^e} \mathbf{B}^{e\mathrm{T}}\mathbf{D}_a\mathbf{B}^e \,\mathrm{d}\Omega, \quad a = 1,2,3,4,5. \tag{15}$$

The global stiffness matrix $\mathbf{K}$ of the unit cell model is assembled from the local stiffness matrix of the yarns and resin elements, namely

$$\mathbf{K} = \bigcup_j \left(2\hat{\kappa}_{23}^j\hat{\nu}_{12}\mathbf{K}_1^j + [\hat{E}_1^j + 4\hat{\kappa}_{23}^j(\hat{\nu}_{12}^j)^2]\mathbf{K}_2^j + \hat{\kappa}_{23}^j\mathbf{K}_3^j + \hat{G}_{12}^j\mathbf{K}_4^j + \hat{G}_{23}^j\mathbf{K}_5^j\right) + \mathbf{K}_{\mathrm{m}}, \tag{16}$$

where j represents the sequence number of yarns in 3D hybrid woven composites; $\hat{}\nu_{12}^{j}, \hat{E}_{1}^{j}, \hat{\kappa}_{23}^{j}, \hat{G}_{12}^{j}$ and $\hat{G}_{23}^{j}$ are material properties of the j-th yarn; and $\mathbf{K}_{1}^{j}, \mathbf{K}_{2}^{j}, \mathbf{K}_{3}^{j}, \mathbf{K}_{4}^{j}$ and $\mathbf{K}_{5}$ represent the assembled constant matrices for the j-th yarn, while $\mathbf{K}_{\mathrm{m}}$ denotes the contribution in assembled global stiffness matrix coming from the resin. It can be seen that Eq.(16) formulates a separated representation of the stiffness matrix as a multidimensional function of various material properties.

3.1.2. Solving procedure of the proper generalised decomposition method in the offline phase

For simplicity and clarity in notation, the material properties for the yarns are denoted by a vector μ,

$$\mu = \{\mu_1, \ldots, \mu_i, \ldots, \mu_n\} = \{\hat{\nu}_{12}^{j}, \hat{E}_{1}^{j}, \hat{\kappa}_{23}^{j}, \hat{G}_{12}^{j}, \hat{G}_{23}^{j}\}_{j=1}^{N_{\mathrm{yarn}}}, \tag{17}$$

where N_{yarn} is the total number of yarns, the parameter μ_i represents those corresponding material properties of each yarn in Eq. (16), and n denotes the total number of parameters in μ. It is trivial to identify that $n = 5N_{\mathrm{yarn}}$. This means the possible combination of yarn material properties forms a $5N_{\mathrm{yarn}}$ dimensional parameter space, which would be impractical to solve Eq. (3) in a traversal approach with conventional iterative algorithms.

In this context, the unknown nodal displacement vector, which can be written as a function of the parameters, is given by $\mathbf{u}_{\mathrm{F}} = \mathbf{u}_{\mathrm{F}}(\mu)$. To address this high-dimensional problem originated from Eq. (3), the PGD method introduces a separated representation to approximate $\mathbf{u}_{\mathrm{F}}(\mu)$ by assuming that it can be approximated by a superposition of M truncated modes, namely

$$\mathbf{u}_{\mathrm{F}}(\boldsymbol{\mu}) \approx \mathbf{u}_{\mathrm{PGD}}^{M}(\boldsymbol{\mu}) := \sum_{m=1}^{M} \mathbf{S}_{0}^{m} \prod_{i=1}^{n} \omega_{i}^{m}(\mu_i). \tag{18}$$

Here, $\mathbf{u}_{\mathrm{PGD}}^{M}(\boldsymbol{\mu})$ approximates $\mathbf{u}_{\mathrm{F}}$ with M modes. Each mode is composed by a product of independent functions of every parameter; $\mathbf{S}^{m}{}_{0}$ is a displacement-like vector represents the m-th spatial mode; $\omega_{i}{}^{m}(\mu_i)$ is the separated one-dimensional function, known as the parametric mode, of the i-th parameter in the m-th mode. It can be further approximated using a one-dimensional basis for discretised calculations:

$$\omega_{i}^{m}(\mu_i) = \mathbf{N}_{i}^{\mathrm{T}}(\mu_i)\mathbf{S}_{i}^{m}, \tag{19}$$

where $\mathbf{N}_i(\mu_i)$ is the interpolation basis vector of the i-th parameter; $\mathbf{S}^{m}{}_{i}$ represents the parametric mode vector related to the corresponding parameter μ_i. Apparently, the separated stiffness matrix can be represented by $\mathbf{K} = \mathbf{K}(\mu)$.

By replacing the nodal displacement vector $\mathbf{u}_{\mathrm{F}}$ in Eq. (5) with $\mathbf{u}^{M}{}_{\mathrm{PGD}}$ and introducing a test function $\mathbf{v}(\mu)$, which has the similar form to $\mathbf{u}^{M}{}_{\mathrm{PGD}}$, we obtain the PGD generalised weak form of Eq. (5) through integrating over the parameter space:

$$\int_{I_{\mu_1}} \cdots \int_{I_{\mu_n}} \mathbf{v}^{\mathrm{T}}(\boldsymbol{\mu}) \mathbf{K}_{\mathrm{F}}(\boldsymbol{\mu}) \mathbf{u}_{\mathrm{PGD}}^{M}(\boldsymbol{\mu}) \, \mathrm{d}\mu_1 \cdots \mathrm{d}\mu_n = - \int_{I_{\mu_1}} \cdots \int_{I_{\mu_n}} \mathbf{v}^{\mathrm{T}}(\boldsymbol{\mu}) \mathbf{K}^{\mathrm{T}}_{\mathrm{EF}}(\mu) \bar{\mathbf{u}}_{\mathrm{E}} \, \mathrm{d}\mu_1 \cdots \mathrm{d}\mu_n. \tag{20}$$

Note that the material property ranges for all candidate materials define a parameter space for each yarn, which remains consistent across all yarns. A suitable ranges of yarn material properties can be selected according to all the calculated yarn material properties using Eq. (1), allowing for reasonable fluctuations in the fibre material as demonstrated in Ref.[44]. Fibre types not listed in Table 1 may still qualify as viable candidates, provided that their properties fall within the prescribed material property ranges. By substituting Eq.(4), (16) and (18) into Eq.(20), the multiple integrals on both sides are simplified to be a multiplication of integrals with a single parameter. Therefore, the spatial mode vector $\mathbf{S}^{m}{}_{0}$ and parametric mode vectors $\mathbf{S}^{m}{}_{i}$ can be solved sequentially using a greedy strategy that solves a rank-one term at a time. The detailed procedure is introduced in [27, 28, 29]. It is noted that the mode by mode calculation for solving Eq.(20) dominates the computational cost in the offline phase of the reduced order modelling.

To control the approximation accuracy in the process of solving Eq.(20), we define the amplitude of the m-th mode β^m

$$\beta^m = \|\mathbf{S}_0^m\| \prod_{i=1}^{n} \|\mathbf{S}_i^m\|, \tag{21}$$

where $\| \bullet \|$ denotes the L^2 norm of $\bullet$ in the corresponding space. To determine an appropriate truncation number of modes M, a stagnation condition of the amplitude is defined as

$$\frac{\beta^M}{\beta^0} < \eta, \tag{22}$$

where η is a user-specified truncation tolerance that controls the accuracy of the produced reduced order model. Higher precision will be achieved by decreasing the tolerance η. As a consequence, the number of modes required will increase and so will the computational cost. For Load case I (Warp tension) in Subsection 4.2, when the tolerance η was set to 1×10^{-3}, the model achieved a computational time of 12.5 hours with a mode count of 44. For the 1,000 randomly generated datasets, the maximum relative error of ν_{xy}^{eff} reached 21%. However, when η was decreased to 5×10^{-4}, the computational time increased to 41.8 hours, while the mode count doubled to 87. Under these revised conditions, the maximum relative error of ν_{xy}^{eff} was significantly reduced to 9%. It shows that an appropriate trade-off between accuracy and cost has to be achieved from empirical knowledge of a particular problem.

Having obtained the PGD modes, a further compression process is performed to refine the reduced order model. This consists of a least-squares projection of $\mathbf{u}^{M}{}_{\mathrm{PGD}}$ onto the same approximation space to filter the redundant information. Further details about this approach can be found in [29, 53].

3.1.3. Encapsulated online phase of the reduced order model

In order to obtain homogenised effective material properties from the mesoscopic unit cell model, the three load cases introduced in Subsection 2.2 require three corresponding offline phases to obtain the separated representations for each load case. By incorporating Eq.(18), the unknown nodal displacement vectors for the three load cases in Eq.(5) can be expressed by

$$\mathbf{u}_{\mathrm{F,I}}(\mu) \approx \sum_{m=1}^{M} \mathbf{S}_{m0,\mathrm{I}} \prod_{i=1}^{n} \mathbf{N}_{\mathrm{T}i}(\mu_i)\mathbf{S}_{mi,\mathrm{I}};$$

$$\mathbf{u}_{\mathrm{F,II}}(\boldsymbol{\mu}) \approx \sum_{m=1}^{M} \mathbf{S}^{m} \prod_{i=1}^{n} \mathbf{N}^{\mathrm{T}}(\mu_i)\mathbf{S}^{m} \quad \begin{matrix} 0,\mathrm{II} \\ i,\mathrm{II} \end{matrix}; \tag{23}$$

$$\mathbf{u}_{\mathrm{F,III}}(\mu) \approx \sum_{m=1}^{M} \mathbf{S}_{m0,\mathrm{III}} \prod_{i=1}^{n} \mathbf{N}_{\mathrm{T}i}(\mu_i)\mathbf{S}_{mi,\mathrm{III}}.$$

Finally, the desired effective properties can also be obtained in terms of functions of the material parameters by recalling Eq.(6) to (9). For instance, we may have

$$E_x^{\mathrm{eff}}(\boldsymbol{\mu}) = \frac{1}{V\varepsilon^0} R_{x,\mathrm{I}}(\boldsymbol{\mu}), \text{ where } R_{x,\mathrm{I}}(\mu) \in \mathbf{r}_{\mathrm{E,I}}(\mu) = \mathbf{K}_{\mathrm{E,I}}(\mu)\bar{\mathbf{u}}_{\mathrm{E,I}} + \mathbf{K}_{\mathrm{EF,I}}(\mu)\mathbf{u}_{\mathrm{F,I}}(\mu). \tag{24}$$

With encapsulating the data of the spatial modes $\mathbf{S}^{m}{}_{0}$ and parametric modes $\mathbf{S}^{m}{}_{i}$ of all three load cases into the reduced order model, we can achieve a much faster calculation during the online phase. Because now for each given set of input parameters μ, it requires only a few matrix-vector multiplication and summations to obtain the effective properties, as demonstrated in Eq. (24), rather than solving a linear system in Eq. (5). So far, an efficient reduced order model, which connects the parameter set μ and the effective properties $\{E_x^{\mathrm{eff}}, \nu_{xy}^{\mathrm{eff}}, E_y^{\mathrm{eff}}, G_{xy}^{\mathrm{eff}}\}$ via simple algebraic functions, has been successfully developed using the PGD method, allowing the rapid generation of the effective properties of various hybridisations of 3D hybrid woven composites within the inverse design framework.

The multiscale computational homogenisation approach [32, 54] based on finite element modelling is a theoretically rigorous alternative to experimental tests, which has been widely used and validated in the characterisation of 3D woven composites [48, 55, 56]. It is noted that uncertainties associated with idealisations in the meso- or microstructural representation, constituent properties for the scale of interest,

and the treatment of material interfaces would affect the predicted results, whilst the effective stiffness is less sensitive than local stress levels as the it still reliably predicted effective stiffness with relative errors of less than 0.58% relative to experimental data in [57]. As this paper is aiming at developing a computational framework for material and configuration selection in inverse design, further validation against experimental results is out of scope and yet to be performed in future work. However, the implementation of such a homogenisation approach is strictly performed by using the specially developed software TexGen [58] for textile composites. In addition, the reduced order model based on proper generalised decomposition (PGD) used to improve computational efficiency, which is rigorously derived from the finite element model with user-specified error control [27]. As a verification, the predicted results are compared with the finite element model within user-specified accuracy before the implementation of the inverse design framework.

3.2. Multi-objective optimisation through genetic algorithm

For a set of material properties μ, the four independent effective properties will be calculated simultaneously. Consequently, the inverse design task can be formulated as a multi-objective optimisation problem. In this work, a genetic algorithm is implemented as the core of the inverse design framework. The tailored effective properties, which are user input of the framework, are treated as multiple optimisation objectives, while the genetic algorithm seeks to identify the optimal hybridisation of 3D hybrid woven composites, as the output of the framework, whose effective properties closely match the tailored ones.

3.2.1. Process of multi-objective optimisation

For each design objective, which is an independent effective property, we introduce an alternative variable $\bar{\theta}_i$, referring to the i-th independent effective property ($\bar{E}_x^{\text{eff}}, \bar{\nu}_{xy}^{\text{eff}}, \bar{E}_y^{\text{eff}}, \bar{G}_{xy}^{\text{eff}}$). Then we define an objective function $\epsilon_i(\mu)$ as the relative error of each identified property $\theta_i(\mu)$, (with i = 1,2,3,4 corresponding to $E_x^{\text{eff}}, \nu_{xy}^{\text{eff}}, E_y^{\text{eff}}, G_{xy}^{\text{eff}}$, respectively), namely

$$\epsilon_i(\boldsymbol{\mu}) = \frac{|\theta_i(\boldsymbol{\mu}) - \bar{\theta}_i|}{|\bar{\theta}_i|} \quad . \tag{25}$$

For simplicity, we use a vector $\epsilon(\mu) = \{\epsilon_1,\epsilon_2,\epsilon_3,\epsilon_4\}$ to denote the objective functions of the four independent effective properties.

Following the weight-based genetic algorithm [21], we define a multi-objective function Ψ in Eq.(26) to evaluate the weighted sum of the relative errors between the effective properties of candidate hybridisations and those of the tailored ones. A smaller value of this multi-objective function indicates that the effective properties of an identified hybridisation more closely match the tailored ones. Thus, the multi-objective optimisation problem is formulated to find a μ^* that minimises the value of the multi-objective function, namely

$$\mu^* = \underset{\mu}{\operatorname{argmin}} \Psi(\mu) = \epsilon(\mu) w^{\mathrm{T}}, \tag{26}$$

where $w = \{w_1, w_2, w_3, w_4\}$ represents the weights for the corresponding effective properties, $\sum_{i=1}^{4} w_i = 1$. The weights are served as input parameters in the framework, decided by designers according to specific requirements; if there is no clear precision preference for a particular engineering constant, it is recommended to assign equal weights to obtain a balanced preference among all objectives. Note that the minimum value of the multi-objective function $\Psi(\mu)$ could be zero, if the minimum value of each objective function $\epsilon_i(\mu)$ is zero.

In the multi-objective optimisation process, different objectives may exhibit conflicting optimisation trends, making it inherently impossible to identify a design point that can optimise all design objectives. As a result, the optimal design is no longer a single solution but a collection of solutions, which are referred to as Pareto optimal solution sets [20]. Each solution within the Pareto optimal solution sets represents a viable option. A genetic algorithm [20] is widely used to perform a global search for these Pareto optimal solution sets within the design space. To control the outputs of the Pareto sets, a constraint value Ψ_c is defined. Only an objective function value below Ψ_c is considered for output. If no candidate meets this constraint threshold, the constraint value can be increased.

In the process of genetic algorithm, a random population of candidate hybridisations of 3D woven composites evolves over successive generations through genetic operators such as selection, crossover, and mutation. The algorithm halts when a multi-objective function tolerance Ψ_{tol} is met or the maximum number of iterations N is reached. Each individual in the population is encoded as a chromosome, representing a potential solution to the problem, and its fitness is evaluated based on the predefined multi-objective function. The fitter individuals are more likely to be selected as parents for the next generation, ensuring the survival of the most promising solutions. The effective properties of the candidate hybridisations are calculated using the reduced order model during the online phase, taking advantage of its enhanced efficiency. It is important to note that each chromosome is decoded into a set of material properties of each yarn μ in the online phase. The procedure of the genetic algorithm for multi-objective optimisation is expressed in Algorithm 1. The encoding strategy, and the genetic operators are described in the following.

3.2.2. Encoding strategy of 3D hybrid woven composites

In the genetic algorithm, the chromosome is introduced as a sequence of N_{yarn} genes. Each gene acts as a discrete variable that labels the material type of a yarn, selected from the ten candidate fibre materials listed in Table 1, encoded with an integer digit from [0,9]. Subsequently, a complete chromosome describes a specific material selection for each yarn in a hybridisation of the 3D hybrid woven composite, with the

345 j-th gene specifying the material for the j-th yarn. The encoding strategy of a chromosome in 3D hybrid woven composites is illustrated in Figure 2(a).

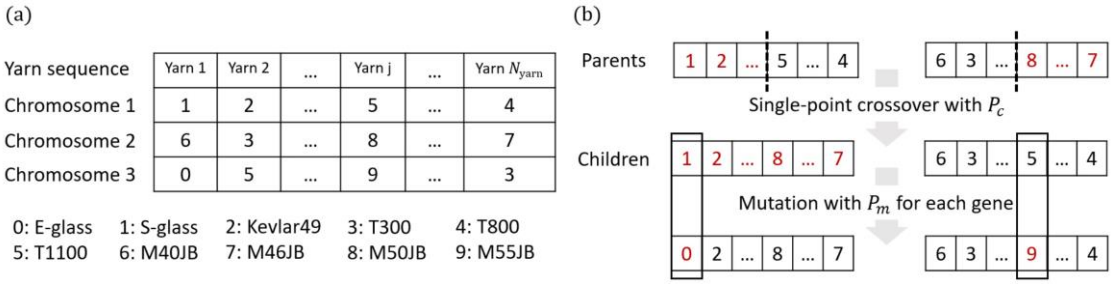

Figure 2: The encoding strategy, single-point crossover operator and mutation operator in genetic algorithm: (a) The encoding strategy of chromosomes in 3D hybrid woven composites; (b) The process of single-point crossover operator and mutation operator.

Algorithm 1: Procedure of genetic algorithm for multi-objective optimisation.

Input: $\bar{E}_x^{\text{eff}}, \bar{\nu}_{xy}^{\text{eff}}, \bar{E}_y^{\text{eff}}, \bar{G}_{xy}^{\text{eff}}$, the tailored effective properties; w, the weights; N, the maximum number of iterations; s, the population size; P_c, the crossover rate; P_m, the mutation rate.

Output: Pareto optimal solution set $\{X_k\}$.

1 encode the candidate materials as genes;

2 generate s potential chromosomes randomly and save them in the population pop;

3 **for** $i = 1$ **to** N **do**

```
    decode pop as multiple sets of μ and calculate corresponding E_x^eff, ν_xy^eff, E_y^eff, G_xy^eff;
    calculate multi-objective function Ψ by Eq.(26) for each individual;
    if min(Ψ) ≤ Ψ_tol then
        break;
    endif
    save those chromosomes with a Ψ < Ψ_c in Pareto optimal solution set {X_k};
    calculate fitness value Φ = 1/Ψ for each chromosome and generate a normalised Roulette wheel;
    for i = 1 to s/2 do
        randomly select two individuals X_A and X_B from pop using the roulette wheel;
        generate X_C and X_D by single-point crossover to X_A and X_B with probability P_c;
        save X_C and X_D to pop1;
    endfor
    for k = 1 to s do
        select a chromosome X_k from pop1;
        mutate each gene of X_k under rate P_m and generate a new X'_k;
        update X_k with X'_k in pop1;
    endfor
    update pop ← pop1;
    update i ← i + 1;
endfor
```

3.2.3. Genetic operators

To search for optimal solutions in a design space, the genetic algorithm employs selection, crossover and mutation operators to mimic the evolutionary process. For the selection operator, the fitness value Φ for each individual hybridisation is calculated as $\Phi = 1/\Psi$ and normalised to form a roulette wheel to probabilistically select two individuals as parents for the crossover. In this roulette wheel selection process, individuals with higher fitness will have a greater chance of being selected as parents, which promotes the survival of the fittest and helps maintain population diversity.

For the crossover operator, a single point is selected at a random location between two genes of the parental chromosomes. Once the point is selected, the chromosomes of both parents are split at this location. The left portion of one is then combined with the right portion of another to generate two children, and this process is repeated to create a new population of individuals. This process is illustrated in Figure 2(b). In order to balance the exploration of new solutions and the exploitation of existing ones, a crossover rate P_c is used to control the frequency of gene exchange.

The mutation operator is designed to maintain genetic diversity within the population by introducing random changes in the chromosomes of individuals following crossover. Each gene has a small mutation probability P_m of mutating to a randomly selected value within the range [0,9], as shown in Figure 2(b). This operation improves the performance of searching for the global optimal by helping the genetic algorithm escape local optima and exploiting unexplored areas within the design space.

4. Case study

In this section, the proposed framework for the inverse design of constituent materials for tailored effective properties is verified through a detailed case study of 3D hybrid woven composites. Firstly, the unit cell model of the studied composites is created, based on which a reduced order model has been generated using the PGD method. This reduced order model is then employed as a rapid predictor of effective properties in the proposed framework to replace the full order model using conventional multiscale approaches. Finally, we employ a genetic algorithm as an optimiser to identify hybridisation options for the unit cell whose effective properties closely match the user-defined values.

4.1. Unit cell model of the 3D hybrid woven composites and associate design space

3D hybrid woven composites of an orthogonal weave pattern with 2 layers of the warp yarns and 3 layers of the weft yarns are used in this case study. The unit cell model of the studied composites is established using the software package TexGen [58], with the corresponding geometric parameters detailed in Table 2. An unstructured tetrahedral mesh with linear elements (207,099 C3D4 elements) is generated using TexGen, and transferred to Abaqus Standard 2024 for subsequent finite element analyses.

In practical applications, changes in material type (e.g. from carbon fibre to glass fibre) may result in variations in yarn geometry (mainly cross-section) due to the differences in fibre diameters and filament count of the used yarns, along with the overall fibre volume fraction. In this study, fibre diameters are included in Table 1 and the intra-yarn fibre volume fraction V^{f} for each yarn type is calculated by its fibre diameter, filament count and cross-section area of the yarn. In this approach, the variation of fibre volume fraction for different yarns can be considered, and the fibre volume fraction is the most critical factor in determining the stiffness of the materials. However, as limited by the current PGD method, we still assume a constant yarn cross-section, which is also adopted by other study [12]. Although this makeshift in constant cross-section may influence local stress distributions, it does not undermine the prediction of stiffness as variation of fibre volume fraction for different yarns has been accounted for in the varied intra-yarn fibre volume fractions.

Based on the yarn geometric parameters presented in Table 2, the cross-sectional area of Z-binders is about 1/4 that of warp and weft yarns. Consequently, the number of filaments in Z-binders is set to 1/4 that of warp and weft yarns to ensure that the V^f is the same with a material type. Please note that this assumption here is for simplicity in demonstrating the workflow only, although different warp, weft and binder yarns can have different cross-sections and V^f for different materials. Consequently, we can determine the V^f based on different fibre diameters in Table 1 and filament count in the yarns. However, an idealised yarn geometry is adopted in the study, introducing additional matrix-rich regions that reduce the overall fibre volume fraction of the unit cell. To compensate, a higher V^f is adjusted to match the overall unit cell fibre volume fraction as closely as possible to the practical material. It should be emphasised that the V^f used here can be substituted with the actual value, as long as the predicted stiffness of the unit cell is not influenced. By substituting V^f into Eq.(1), we present the calculated elastic properties of various yarns with different filament counts and V^f values, along with their genetic codes in the genetic algorithm in Table 3. For example, if warp and weft yarns are chosen as 12K and Z-binder is selected as 3K with a fibre diameter being 0.007 mm, the fibre volume fraction for this unit cell is 45.9%, which is derived geometrically from the unit cell configuration. In addition, it is demonstrated in [59] that a reduced order model taking into account variable geometric parameters can also be achieved. The challenge of addressing varying geometric dimensions warrants further exploration in future research.

Table 2: Geometric parameters of the 3D orthogonal woven composite (Unit for dimensions: mm).

Type of yarns	Volume fraction (%)	Section	Spacing	Width	Height
Warp yarns	16.6		2	1.8	0.33
Weft yarns	33.2	Power ellipse*	2.4	1.8	0.33
Z-binders	3.0		1.19	0.99	0.15

*The power ellipse section power is 0.4.

As the unit cell model in this case study has 12 yarns, if the material of each yarn can be selected from the ten listed in Table 3, there will be about 1.0×10^{12} possible hybridisations in the design space. Although this vast design space can be handled by the proposed frame, to demonstrate the workflow, we decrease the size of the problem by introducing some manufacturing restrictions that take into account the weaving process. Considering the loom's operations of lifting the harness and inserting the weft yarn, we define "layers" as a discrete unit. Within each layer, the yarn materials are assumed to be the same. Therefore, there are only 6 layers (including the Z-binders as a single layer) to be designed, decreasing the number of hybridisations to 1.0×10^{6} in this work, and each hybridisation is encoded as a chromosome with six digits,

as detailed in Figure 3. Note that the simplification of the design space from 1.0×10^{12} to 1.0×10^{6} may potentially overlook the possibility of a single weft layer containing two separate yarns and thus missing a true global optimum for the hybrid material. For real applications, all possible combinations should be considered but it would lead to an increased computational cost.

Table 3: Elastic properties of candidate yarns calculated by Eq. (1) with different filament counts and V^f (Unit for moduli: GPa).

Codes	Yarn	Filamentcount		V^f	E_1	E_2	ν_{12}	ν_{23}	G_{12}	G_{23}
		Warpandweft	Z-binder							
0	E-glass	12K	3K	87.0%	61	30.7	0.22	0.29	11.9	11.9
1	S-glass	12K	3K	87.0%	76	33.4	0.25	0.31	12.8	12.8
2	Kevlar49	4K	1K	85.2%	96	33.1	0.36	0.35	12.2	12.2
3	T300	12K	3K	87.0%	200	11.5	0.22	0.27	6.4	4.5
4	T800	24K	6K	88.8%	261	14.0	0.22	0.27	10.5	5.5
5	T1100	24K	6K	88.8%	288	15.4	0.22	0.27	9.7	6.0
6	M40JB	24K	6K	88.8%	335	17.2	0.22	0.28	10.6	6.7
7	M46JB	24K	6K	88.8%	387	15.7	0.22	0.28	10.9	6.2
8	M50JB	24K	6K	88.8%	422	16.9	0.22	0.28	10.9	6.6
9	M55JB	24K	6K	88.8%	480	18.5	0.22	0.28	10.9	7.2
Range					[61, 480]	[11.5, 33.4]	[0.22, 0.36]	[0.27, 0.35]	[6.4, 12.8]	[4.5, 12.8]

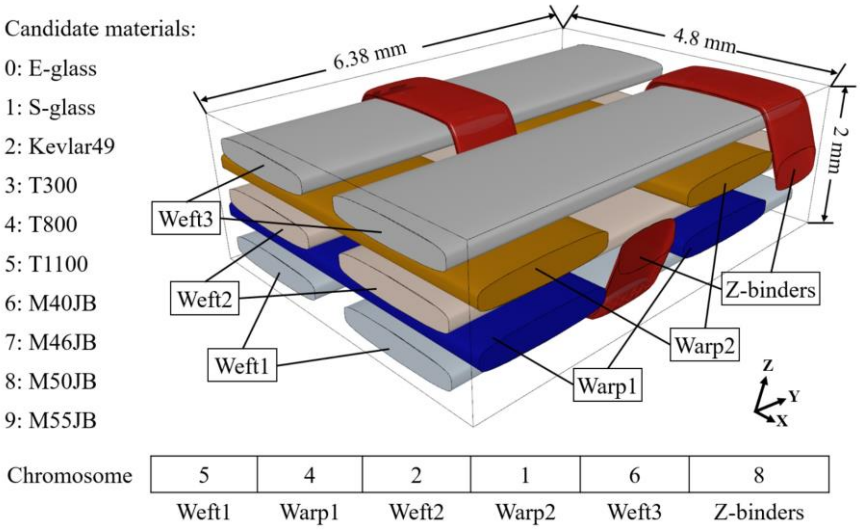

Figure 3: The unit cell of the studied 3D hybrid woven composite and an example of its chromosome encoding.

4.2. Verification of the generated reduced order model for effective properties

Based on the mesh of the unit cell, the global stiffness matrix is separated as a sum of matrices and the material parameters of each layer are extracted in the form of Eq. (16). The material type of each layer is considered

independent, and the ranges of material parameters for all material types are displayed in Table 3. By feeding these parametric ranges for each layer into Eq. (20), a reduced order model has been obtained by the PGD method under three load cases (with load case I,II,III representing warp tension, weft tension and in-plane shear, respectively), which is used to efficiently generate effective properties for different hybridisations. The inputs of this reduced order model are the material properties of each layer μ, and the outputs are the corresponding effective properties. In the genetic algorithm, the layers of the unit cell for a hybridisation is encoded as a chromosome; thus, we decode the chromosome as a set of material properties μ in the online phase of the reduced order model. It is important to emphasise that the inputs for this reduced order model consist of either a set of μ or multiple sets of μ. This flexibility showcases the capability of this reduced order model to simultaneously accommodate diverse hybridisations of 3D hybrid woven composites.

The evolution of the modal amplitudes for three load cases has been shown in Figure 4. To optimise computational efficiency while maintaining accuracy, we set the truncation tolerance $\eta = 5\times10^{-4}$. This value ensures that the PGD solution for all three load cases achieving the same accuracy with the least number of modes. As the number of modes increases, the corresponding modal amplitudes decrease progressively.

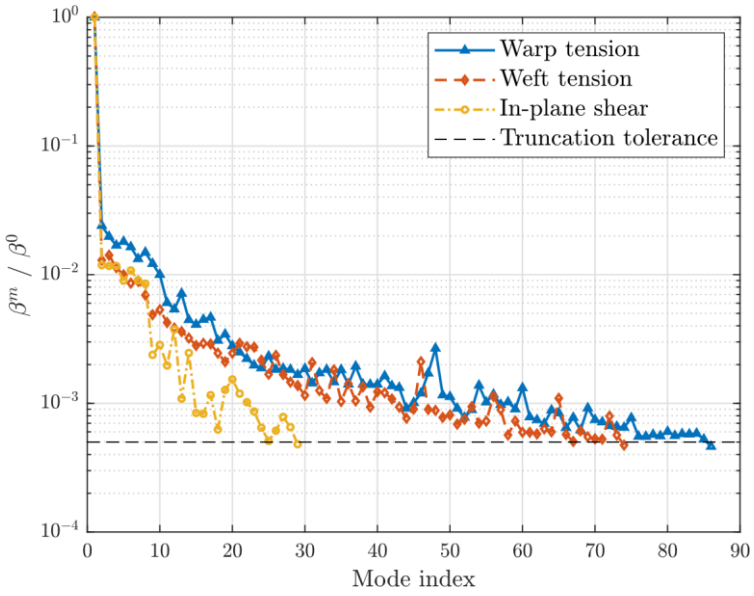

Figure 4: Evolution of modal amplitudes of the three load cases for effective properties with truncation tolerance $\eta = 5\times10^{-4}$.

The total number of modes is determined once the convergence criterion defined in Eq.(22) is satisfied. In particular, the number of truncated modes varies significantly among different load cases, as each load case involves a different stiffness matrix in Eq. (20), resulting in different modal characteristics. Of particular

interest, the in-plane shear load case exhibits the fastest convergence rate among the three cases, requiring fewer modes to achieve the convergence criterion than the other two cases. The offline phase computation for the reduced order model was performed on a supercomputer equipped with Hygon C86 7285 32-core processors. Each of the three load cases was configured to use 1 node with 256 GB DDR4 RAM, and only

3 cores. This is because the memory requirement of the unit cell model is demanding, while the PGD approach is a sequential process. The computational times for the three load cases are 42.8, 35.1, and 9.6 hours, corresponding to warp tension, weft tension and in-plane shear, respectively. Assuming all yarns are of type T300 and accounting for the material property variability reported in [44] (±0.01 GPa for moduli and ±0.01 for Poisson's ratios), the relative errors for the homogenised properties are found to be within

0.01% for the moduli and 3% for Poisson's ratios. The relative errors for Poisson's ratios are higher than those of moduli, which can be attributed to the greater inherent variability in Poisson's ratios as reported in the material properties.

As a verification of the reduced order model, we randomly selected 1,000 hybridisations within the design space to assess its accuracy. The effective properties calculated by the reduced order model and the full order model using conventional homogenisation approach are populated for each hybridisation, and then compared in terms of the relative error. The results are illustrated in Figure 5. The analysis demonstrates

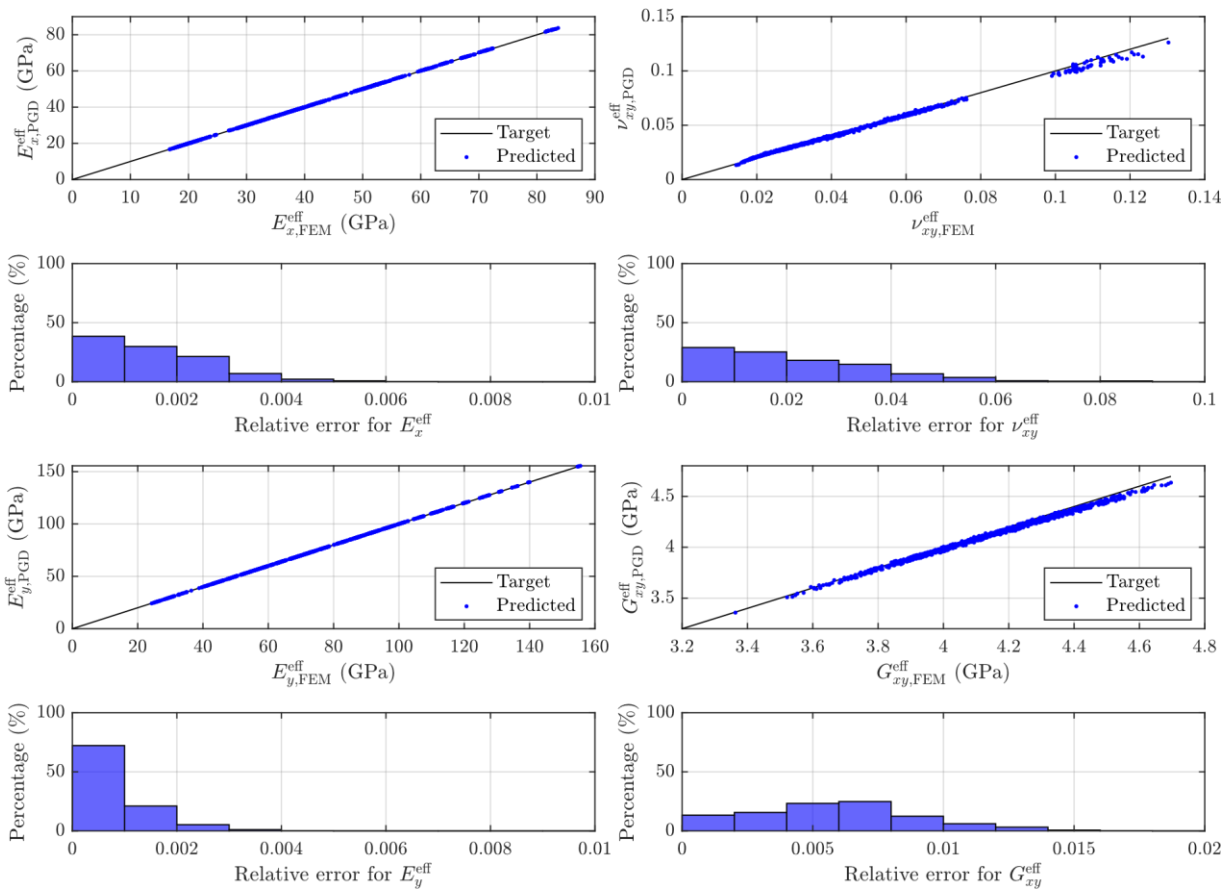

Figure 5: Verification of the reduced order model: predicted versus reference values of the effective properties for 1,000 random hybridisations within the design space, alongside the corresponding range of relative errors.

that the relative errors of the effective moduli are constantly maintained within a 2% deviation from the reference solutions. However, the relative errors for Poisson's ratio ν_{xy}^{eff} exhibit relatively higher values, which is a phenomenon consistent with Ref. [30]. Specifically, 95% of the hybridisations exhibit relative error for ν_{xy}^{eff} below 5%, with the maximum error peaking at 9%. Notably, the hybridizations predominantly featuring medium modulus fibres in both warp and weft yarns (e.g., 526652 and 554560) achieved a relative error of 9% for ν_{xy}^{eff}. This discrepancy can be attributed to the fact that the computation of effective moduli in Eq.(24) includes an additive term irrelevant to the unknown displacements ($\mathbf{K}_{\text{E}}\bar{\mathbf{u}}_{\text{E}}$) for the reaction forces. Consequently, during the propagation of errors associated with the unknown displacements, the denominator of the relative errors for effective moduli becomes disproportionately larger than that of Poisson's ratio.

In addition, we have discovered another situation in which the relative errors of the effective properties

exhibit errors approximately 100 times greater than the truncation tolerance η in the PGD method. This phenomenon results from the macroscopic strain ε^0 (with a value of 0.01) serving as the denominator in the calculation process for the effective properties, as defined by Eq.(9).

4.3. Implementation of genetic algorithm for multi-objective optimisation

A comprehensive review of genetic algorithms [60] has identified that optimal solutions can be found within 100 generations when the population size is set to 50. In this specific application of the genetic algorithm, a generation limit of 100 was implemented, coupled with a population size of 50. According to Ref. [61], we took the crossover rate P_c = 0.8 and the mutation rate P_m = 0.05 in this case study. In the iterative process of the genetic algorithm, we define the termination criteria as either the minimum value of the multi-objective function falling below 0.001 or the number of iterations reaching a maximum limit 100. In the outputs of the framework, the value of Ψ_c is initialised as 0.05. If no results are obtained within the initial Ψ_c, it will gradually increase by a step of 0.01 until the results are obtained. For convenience of display, we only plot three of those solutions with lowest multi-objective function values in ascending order for the following radar figures.

For a specific unit cell, the framework automatically identifies optimal hybridisations by selecting from a pool of candidate materials, enabling the creation of multiple hybridisations that closely match the tailored effective properties. The material properties of the candidate material are discretely defined and the material selection of each yarn in the unit cell is independent. This results in effective properties within the design space that are inherently discrete. If the tailored effective properties are not sufficiently feasible to be achieved, the framework would provide some hybridisations whose effective properties meet the requirements as closely as possible. By adjusting the weights for the tailored effective properties, it is possible to ensure that a specific property of interest matches the tailored value better than others in the identified hybridisations.

4.4. Verification of the implementation of the inverse design framework

To verify the implementation of the proposed framework, a "sanity check" [32] is performed with a set of tailored effective properties $\bar{E}_x^{\text{eff}}$ = 38.139 GPa, $\bar{\nu}_{xy}^{\text{eff}} = 0.0283$, $\bar{E}_y^{\text{eff}} = 68.451$ GPa, $\bar{G}_{xy}^{\text{eff}}$ = 3.152 GPa. These values are computed via standard homogenisation method by setting all yarn materials in the unit cell to be T300. A uniform weight is chosen as w = {0.25,0.25,0.25,0.25}. The output hybridisations with Ψ_c = 0.05 are presented in Figure 6, and the number of total identified hybridizations is 10. Among the

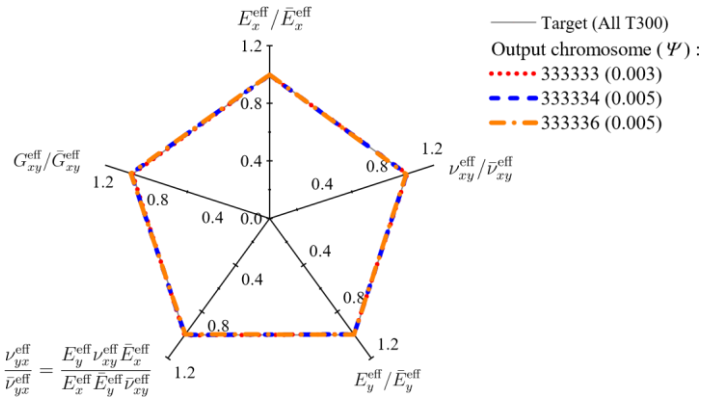

Figure 6: Output hybridisations for sanity check with tailored effective properties $\bar{E}_x^{\text{eff}}$ = 38.139 GPa, $\bar{\nu}_{xy}^{\text{eff}}$ = 0.0283, $\bar{E}_y^{\text{eff}}$ = 68.451 GPa, $\bar{G}_{xy}^{\text{eff}}$ = 3.152 GPa, w = {0.25,0.25,0.25,0.25} and Ψ_c = 0.05; the number of total identified hybridizations is 10.

hybridisations identified from the framework, it is shown that the target hybridisation, with chromosome 333333, minimises the multi-objective function to be Ψ = 0.003. This corresponds to the non-hybrid solution where all yarn materials are set as T300. Furthermore, other hybridisations, with chromosome 333334 or 333336, demonstrating effective properties similar to the tailored ones, have also been identified with Ψ = 0.005.

4.5. Results and discussion

The framework has demonstrated remarkable capability in systematically optimising material arrangements to achieve a variety of tailored effective properties, as shown in Figure 7. When lower $\bar{E}_x^{\text{eff}}$ and $\bar{E}_y^{\text{eff}}$ are preferred by the users, as shown in Figure 7(a), the optimised hybridisations incorporate a greater proportion of lower modulus materials. Conversely, when higher $\bar{E}_x^{\text{eff}}$ and $\bar{E}_y^{\text{eff}}$ are requested, as shown in Figure 7(b), the framework prioritises the inclusion of more brittle and higher modulus materials in the identified hybridisations, which could negatively impact the toughness. This systematic variation of material constituents underscores the framework's ability to design 3D hybrid woven composites with precisely tailored mechanical properties, offering both flexibility in achieving desired moduli and control over corresponding Poisson's ratios.

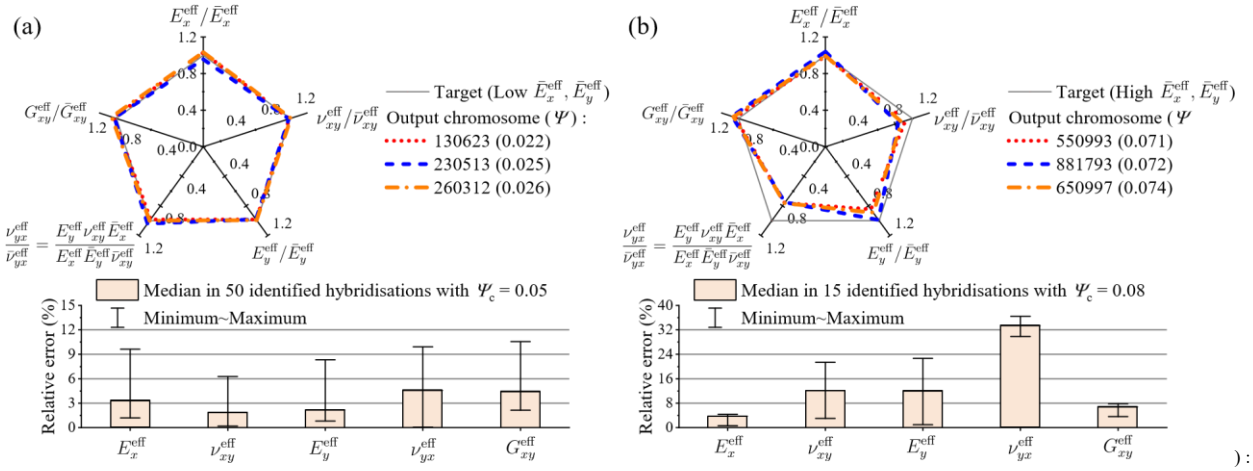

Figure 7: Output hybridisations and relative error of each effective property for different tailored effective properties with w = {0.25,0.25,0.25,0.25} and Ψ_c = 0.05: (a) $\bar{E}_x^{\text{eff}}$ = 50 GPa, $\bar{\nu}_{xy}^{\text{eff}}$ = 0.1, $\bar{E}_y^{\text{eff}}$ = 30 GPa, $\bar{G}_{xy}^{\text{eff}}$ = 4 GPa; (b) $\bar{E}_x^{\text{eff}}$ = 70 GPa, $\bar{\nu}_{xy}^{\text{eff}}$ = 0.03, $\bar{E}_y^{\text{eff}}$ = 110 GPa, $\bar{G}_{xy}^{\text{eff}}$ = 4 GPa.

In order to investigate the impact of weights on results, Figure 8 has compared the results obtained from different weights under the same tailored effective properties: $\bar{E}_x^{\text{eff}}$ = 70 GPa, $\bar{\nu}_{xy}^{\text{eff}}$ = 0.07, $\bar{E}_y^{\text{eff}}$ = 30 GPa, $\bar{G}_{xy}^{\text{eff}}$ = 4 GPa. Figure 8(a) has shown that the obtained E_y^{eff} is not close enough to the target $\bar{E}_y^{\text{eff}}$ with a uniform weight w_1 = {0.25,0.25,0.25,0.25}. By adjusting the weights to w_2 = {0.1,0.1,0.7,0.1}, the new result for E_y^{eff} is significantly improved, as presented in Figure 8(b). The relative error of each effective property for the identified hybridisations in Figure 8(a)(b) were compared in Figure 8(c).

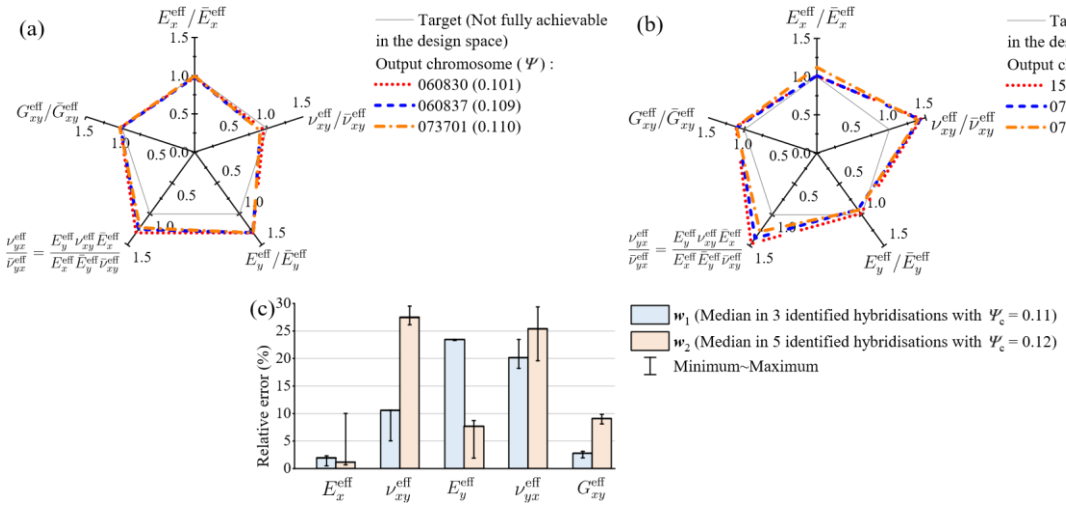

Figure 8: Output hybridisations for different weights with tailored effective properties $\bar{E}_x^{\text{eff}}$ = 70 GPa, $\bar{\nu}_{xy}^{\text{eff}}$ = 0.07, $\bar{E}_y^{\text{eff}}$ = 30 GPa, $\bar{G}_{xy}^{\text{eff}}$ = 4 GPa: (a) w_1 = {0.25,0.25,0.25,0.25} and Ψ_c = 0.11; (b) w_2 = {0.1,0.1,0.7,0.1} and Ψ_c = 0.06; (c) Relative error of each effective property for identified hybridisations with different weights and Ψ_c.

When equal weights are assigned, the optimisation reflects a balanced preference among all objectives, leading to a compromise solution rather than an optimal result for each individual parameter. Increasing the weight of E_y inevitably introduces trade-off in the relative errors of the remaining objectives. As shown in Figure 8(c), Poisson's ratio exhibits a more pronounced variation in relative error compared to E_x and G_{xy}. This behaviour is primarily attributed to its smaller reference magnitude, which amplifies the sensitivity of relative error to small absolute deviations. These characteristics highlight the necessity of careful weight selection, particularly when Poisson's ratio is the primary parameter of interest. This indicates that the proposed framework provides the flexibility to adjust the associated weights when specific effective properties need to be prioritised.

Considering the intricate manufacturing process for 3D woven composites, hybrid composites with less different types of fibre may be preferred if they can already meet the tailored values. To demonstrate the capability of the proposed framework to handle this preference, it is possible to impose a user-defined restriction on the number of constituent materials used. To demonstrate this, under the same tailored effective properties, weights in Figure 7(a) and Ψ_c was set as 0.08, the hybrid composites were restricted to utilise no more than three distinct constituent materials. The corresponding results are presented in Figure 9, and the number of total identified hybridizations is 3. It can be seen that the resulting hybridisations still satisfy the design requirements while restricting the number of constituent materials. In practical applications, the proposed framework can streamline the manufacturing process and enhance overall production efficiency by controlling the number of constituent materials. It is worth noting that these identified hybridisations can be used to reduce the design space to further accelerate the design of more complex mechanical behaviour.

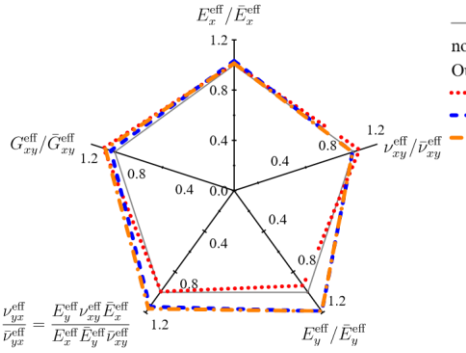

Figure 9: Output hybridisations with no more than three distinct materials. Tailored effective properties, weights are same as Figure 7(a) and Ψ_c is set as 0.08; the number of total identified hybridizations is 3.

In this case study, the conventional numerical homogenisation and the online phase calculation of the reduced order model are performed on a workstation with a 16-core Intel Core i7-1260P processor and 32 GB RAM. To compare the computational efficiency of the two methods, we select the case of Figure 8(a) as an example, where the maximum number of iterations is reached and the effective properties are repeatedly calculated 5,000 times in the inverse design framework. For the full model using the conventional homogenisation method, we performed 100 tests and use the average runtime per test to estimate the total time required for material characterisation. For the reduced order model in the online phase, we represent the actual time. The wallclock times for both methods are listed in Table 4. It can be seen that the computational time of the reduced order model in the online phase results in an acceleration of approximately 122 times compared to the conventional numerical homogenisation. This shows that the conventional numerical homogenisation entails a substantial computational burden, making it impractical for the inverse design framework. However, the utilisation of reduced order model has greatly reduced the computational cost to an acceptable wallclock time.

Table 4: Comparison of wallclock times for Figure 8(a) with effective properties being repeatedly calculated for 5,000 times.

	Wallclock time (s)	Acceleration
Full order model using conventional homogenisation	≈282,000	N/A
Reduced order model in the online phase	2,303	122

5. Conclusions

In order to tailor effective properties of 3D hybrid woven composites through the selection of constituent materials, we propose an efficient inverse design framework to replace the trial-and-error approaches. This framework employs a genetic algorithm as an optimiser to automatically search for optimal combinations of constituent materials, while utilising a rapid PGD-based reduced order model to replace the conventional multiscale method for the forward prediction of effective properties. A case study on 3D orthogonal woven composites, which involves a design space of one million potential combinations of constituent materials, was used to verify the proposed inverse design framework. The results demonstrate that the framework can efficiently identify optimal solutions within the vast design space by increasing computational efficiency of material characterisation. Furthermore, after having addressed the design of stiffness, these optimal solutions can be used to define a reduced design space to further consider more complex mechanical behaviour such as strength.

References

[1] A. P. Mouritz, M. K. Bannister, P. Falzon, K. Leong, Review of applications for advanced three-dimensional fibre textile composites, Composites Part A: applied science and manufacturing 30 (12) (1999) 1445–1461.

[2] S. Yan, X. Zeng, A. Long, Experimental assessment of the mechanical behaviour of 3d woven composite t-joints, Composites Part B: Engineering 154 (2018) 108–113.

[3] G. Marsh, Aero engines lose weight thanks to composites, Reinforced Plastics 56 (6) (2012) 32–35.

[4] Y. Swolfs, I. Verpoest, L. Gorbatikh, Recent advances in fibre-hybrid composites: materials selection, opportunities and applications, International Materials Reviews 64 (4) (2019) 181–215.

[5] W. Hufenbach, M. Gude, C. Ebert, Hybrid 3d-textile reinforced composites with tailored property profiles for crash and impact applications, Composites science and technology 69 (9) (2009) 1422–1426.

[6] R. Mun˜oz, V. Mart´ınez, F. Sket, C. Gonza´lez, J. LLorca, Mechanical behavior and failure micromechanisms of hybrid 3d woven composites in tension, Composites Part A: Applied Science and Manufacturing 59 (2014) 93–104.

[7] M. Pankow, A. Quabili, C.-F. Yen, Hybrid three-dimensional (3-d) woven thick composite architectures in bending, JOM 66 (2014) 255–260.

[8] Q. Liang, J. Liu, X. Wang, X. Liu, D. Zhang, K. Qian, Flexural progressive failure mechanism of hybrid 3d woven composites: Combination of x-ray tomography, acoustic emission and digital image correlation, Composite Structures 280 (2022) 114894.

[9] S. Trimble, GE Aviation reveals new hybrid composites in GE9X, https://www.flightglobal.com/ge-aviation-revea ls-new-hybrid-composites-in-ge9x/116235.article, published date: 2015-03-14, acccessed: 2025-05-18.

[10] M. Pankow, M. Riosbass, B. Justusson, D. Zhang, A. Waas, C. Yen, Effect of fiber hybridization on tensile fracture of 3d woven textile composites, Composites Part A: Applied Science and Manufacturing 165 (2023) 107306.

[11] A. Al-Nadhari, H. Ulus, S. Topal, M. Yildiz, Analyzing stiffness variations in 3d woven composites: A multi-instrumental study on glass/kevlar hybridization effects under tensile and shear loads, Composites Part A: Applied Science and Manufacturing 191 (2025) 108722.

[12] D. Zhang, A. M. Waas, C.-F. Yen, Progressive damage and failure response of hybrid 3d textile composites subjected to flexural loading, part ii: Mechanics based multiscale computational modeling of progressive damage and failure, International Journal of Solids and Structures 75 (2015) 321–335.

[13] S. Yan, X. Zeng, A. Long, Meso-scale modelling of 3d woven composite t-joints with weave variations, Composites Science and Technology 171 (2019) 171–179.

[14] S. J. Kuehsamy, Z.-P. Wang, M. H. Jhon, F. Yang, N. Sridhar, Design optimization of integral stiffeners for 3d woven composite preforms, in: Structures, Vol. 63, Elsevier, 2024, p. 106449.

[15] E. Sitnikova, M. Xu, W. Kong, S. Hu, S. Li, Design strategy for 3d layer-to-layer angle interlock woven composites, Materials & Design 247 (2024) 113414.

[16] X. Sun, L. Yue, L. Yu, C. T. Forte, C. D. Armstrong, K. Zhou, F. Demoly, R. R. Zhao, H. J. Qi, Machine learning-enabled forward prediction and inverse design of 4d-printed active plates, Nature Communications 15 (1) (2024) 5509.

[17] Y. Gao, R. Duddu, S. Kolouri, A. Gupta, P. Prabhakar, An inverse design framework for optimizing tensile strength of composite materials based on a cnn surrogate for the phase field fracture model, Composites Part A: Applied Science and Manufacturing (2025) 108758.

[18] W. Tao, Z. Liu, P. Zhu, C. Zhu, W. Chen, Multi-scale design of three dimensional woven composite automobile fender using modified particle swarm optimization algorithm, Composite Structures 181 (2017) 73–83.

[19] M. Esmaeeli, M. R. Nami, B. Kazemianfar, Geometric analysis and constrained optimization of woven z-pinned composites for maximization of elastic properties, Composite Structures 210 (2019) 553–566.

[20] Q. Wang, X. Yang, H. Zhao, X. Zhang, G. Cao, M. Ren, Microscopic residual stresses analysis and multi-objective optimization for 3d woven composites, Composites Part A: Applied Science and Manufacturing 144 (2021) 106310.

[21] P. Hajela, C.-Y. Lin, Genetic search strategies in multicriterion optimal design, Structural optimization 4 (2) (1992) 99–107.

[22] G. Balokas, S. Czichon, R. Rolfes, Neural network assisted multiscale analysis for the elastic properties prediction of 3d braided composites under uncertainty, Composite Structures 183 (2018) 550–562.

[23] S. Yan, X. Zou, M. Ilkhani, A. Jones, An efficient multiscale surrogate modelling framework for composite materials considering progressive damage based on artificial neural networks, Composites Part B: Engineering 194 (2020) 108014.

[24] G. Rozza, Reduced-basis methods for elliptic equations in sub-domains with a posteriori error bounds and adaptivity, Applied Numerical Mathematics 55 (4) (2005) 403–424.

[25] A. Quarteroni, A. Manzoni, F. Negri, Reduced basis methods for partial differential equations: an introduction, Vol. 92, Springer, 2015.

[26] G. H. Dunteman, Principal components analysis, Vol. 69, Sage, 1989.

[27] F. Chinesta, A. Ammar, E. Cueto, Recent advances and new challenges in the use of the proper generalized decomposition for solving multidimensional models, Archives of Computational methods in Engineering 17 (4) (2010) 327–350.

[28] F. Chinesta, A. Leygue, F. Bordeu, J. V. Aguado, E. Cueto, D. Gonz´alez, I. Alfaro, A. Ammar, A. Huerta, Pgdbased computational vademecum for efficient design, optimization and control, Archives of Computational methods in Engineering 20 (2013) 31–59.

[29] A. Sibileau, A. Garc´ıa-Gonza´lez, F. Auricchio, S. Morganti, P. D´ıez, Explicit parametric solutions of lattice structures with proper generalized decomposition (pgd) applications to the design of 3d-printed architectured materials, Computational Mechanics 62 (2018) 871–891.

[30] M. E. F. Idrissi, F. Praud, V. Champaney, F. Chinesta, F. Meraghni, Multiparametric modeling of composite materials based on non-intrusive pgd informed by multiscale analyses: Application for real-time stiffness prediction of woven composites, Composite Structures 302 (2022) 116228.

[31] K. El-Ghamrawy, Proper generalized decomposition solutions for composite laminates parameterized with fibre orientations for fast computations (2021).

[32] S. Li, E. Sitnikova, Representative volume elements and unit cells: concepts, theory, applications and implementation, Woodhead Publishing, 2019.

[33] J. Michel, H. Moulinec, P. Suquet, Effective properties of composite materials with periodic microstructure: a computational approach, Computer Methods in Applied Mechanics and Engineering 172 (1) (1999) 109–143.

[34] C. C. Chamis, Simplified composite micromechanics equations for hygral, thermal and mechanical properties, in: Ann. Conf. of the Society of the Plastics Industry (SPI) Reinforced Plastics/Composites Inst., no. NASA-TM-83320, 1983.

[35] S. V. Lomov, D. S. Ivanov, I. Verpoest, M. Zako, T. Kurashiki, H. Nakai, S. Hirosawa, Meso-fe modelling of textile composites: Road map, data flow and algorithms, Composites Science and Technology 67 (9) (2007) 1870–1891.

[36] Z. Zou, S. Li, An inverse application of unit cells for extracting fibre properties from effective properties of composites, Mathematics and Mechanics of Solids (2023) 10812865231212150.

[37] Modulus of epoxy resin (ebecryl® 3503), https://chemiteca.com/listing/ebecryl-3503/, acceseed: 2025-08-14.

[38] J. D. Littell, W. K. Binienda, R. K. Goldberg, G. D. Roberts, Full-field strain methods for investigating failure mechanisms in triaxial braided composites, in: Earth & Space 2008: Engineering, Science, Construction, and Operations in Challenging Environments, 2008, pp. 1–12.

[39] Prime™ 20lv-epoxy infusion system, https://www.compositesone.com/wp-content/uploads/2013/07/PRIME-20LV_v10

.pdf, accessed: 2025-05-18.

[40] P. D. Soden, M. J. Hinton, A. Kaddour, Lamina properties, lay-up configurations and loading conditions for a range of fibre reinforced composite laminates, in: Failure criteria in fibre-reinforced-polymer composites, Elsevier, 2004, pp. 30–51. [41] Glass filament diameter-1, https://bgf.com/glass-filament-diameter/, acceseed: 2025-07-31.

[42] Glass filament diameter-2, https://garcomfg.com/wp-content/uploads/2014/02/glass-yarn-nomenclature.pdf, acceseed: 2025-12-17.

[43] S-series™ high performance materials, https://www.rockwestcomposites.com/on/demandware.static/Sites-RWC-Site/Sites-rwc-master-catalog/-/downloads/E-S1-S2-Glass-Properties.pdf, acceseed: 2025-05-18.

[44] N. Yang, Z. Zou, P. Potluri, C. Soutis, K. B. Katnam, Intra-yarn fibre hybridisation effect on homogenised elastic properties and micro and meso-stress analysis of 2d woven laminae: Two-scale fe model, Composite Structures 344 (2024) 118358.

[45] Kevlar aramid fibre technical guide, https://www.dupont.com/content/dam/dupont/amer/us/en/safety/public/documents/en/Kevlar Technical Guide 0319.pdf, acceseed: 2025-07-30.

[46] S.-P. Ng, P.-C. Tse, K.-J. Lau, Numerical and experimental determination of in-plane elastic properties of 2/2 twill weave fabric composites, Composites Part B: Engineering 29 (6) (1998) 735–744.

[47] Data sheets of carbon fibre from toray, https://www.cf-composites.toray/resources/data_sheets/, accessed: 2025-05-18.

[48] T. M. Ricks, B. Farrokh, B. A. Bednarcyk, E. J. Pineda, A comparison of different modeling strategies for predicting effective properties of 3d woven composites, in: AIAA Scitech 2019 Forum, 2019, p. 0692.

[49] J. F. Abel, M. S. Shephard, An algorithm for multipoint constraints in finite element analysis, International Journal for Numerical Methods in Engineering 14 (3) (1979) 464–467.

[50] J. T. Oden, N. Kikuchi, Finite element methods for constrained problems in elasticity, International Journal for Numerical Methods in Engineering 18 (5) (1982) 701–725.

[51] M. Ainsworth, Essential boundary conditions and multi-point constraints in finite element analysis, Computer Methods in Applied Mechanics and Engineering 190 (48) (2001) 6323–6339.

[52] R. Hill, Elastic properties of reinforced solids: Some theoretical principles, Journal of the Mechanics and Physics of Solids 11 (5) (1963) 357–372.

[53] D. Modesto, S. Zlotnik, A. Huerta, Proper generalized decomposition for parameterized helmholtz problems in heterogeneous and unbounded domains: Application to harbor agitation, Computer Methods in Applied Mechanics and Engineering 295 (2015) 127–149.

[54] F. Otero, S. Oller, X. Martinez, Multiscale computational homogenization: review and proposal of a new enhanced-firstorder method, Archives of Computational Methods in Engineering 25 (2) (2018) 479–505.

[55] B. Stier, J.-W. Simon, S. Reese, Comparing experimental results to a numerical meso-scale approach for woven fiber reinforced plastics, Composite structures 122 (2015) 553–560.

[56] D. K. Patel, A. M. Waas, C.-F. Yen, Compressive response of hybrid 3d woven textile composites (h3dwtcs): An experimentally validated computational model, Journal of the Mechanics and Physics of Solids 122 (2019) 381–405.

[57] W. Tao, P. Zhu, C. Xu, Z. Liu, Uncertainty quantification of mechanical properties for three-dimensional orthogonal woven composites. part ii: Multiscale simulation, Composite Structures 235 (2020) 111764.

[58] L. P. Brown, Texgen, in: Advanced Weaving Technology, Springer, 2022, pp. 253–291.

[59] A. Ammar, A. Huerta, F. Chinesta, E. Cueto, A. Leygue, Parametric solutions involving geometry: a step towards efficient shape optimization, Computer Methods in Applied Mechanics and Engineering 268 (2014) 178–193.

[60] Z. Wang, A. Sobey, A comparative review between genetic algorithm use in composite optimisation and the state-of-the-art

685 in evolutionary computation, Composite Structures 233 (2020) 111739.

[61] A. Ehsani, J. Rezaeepazhand, Stacking sequence optimization of laminated composite grid plates for maximum buckling load using genetic algorithm, International Journal of Mechanical Sciences 119 (2016) 97–106.